remote sensing

MDPI

Article

Monitoring and Disaster Assessment of Glacier Lake Outburst in High Mountains Asian Using Multi-Satellites and HEC-RAS: A Case of Kyagar in 2018

Long Jiang [1], Zhiqiang Lin [1,*], Zhenbo Zhou [2], Hongxin Luo [1], Jiafeng Zheng [1], Dongsheng Su [1] and Minhong Song [1]

[1] School of Atmospheric Sciences, Chengdu University of Information Technology, Chengdu 610225, China; 3230101073@stu.cuit.edu.cn (L.J.); 3230101049@stu.cuit.edu.cn (H.L.); zjf1988@cuit.edu.cn (J.Z.); sds@cuit.edu.cn (D.S.); songmh@cuit.edu.cn (M.S.)

[2] Tibet Institute of Plateau Atmospheric and Environmental Science, Meteorological Bureau of Tibet Autonomous Region, Lhasa 850000, China; zhouzb0891@aliyun.com

* Correspondence: linzq@cuit.edu.cn

Abstract: The glaciers in the High Mountain Asia (HMA) region are highly vulnerable to global warming, posing significant threats to downstream populations and infrastructure through glacier lake outburst floods (GLOFs). The monitoring and early warnings of these events are challenging due to sparse observations in these remote regions. To explore reproducing the evolution of GLOFs with sparse observations in situ, this study focuses on the outburst event and corresponding GLOFs in August 2018 caused by the Kyagar Glacier lake, a typical glacier lake of the HMA in the Karakoram, which is known for its frequent outburst events, using a combination of multi-satellite remote sensing data (Sentinel-1 and Sentinel-2) and the HEC-RAS hydrodynamic model. The water depth of the glacier lake and downstream was extracted from satellite data adapted by the Floodwater Depth Elevation Tool (FwDET) as a baseline to compare them with simulations. The elevation-water volume curve was obtained by extrapolation and was applied to calculate the water surface elevation (WSE). The inundation of the downstream of the lake outburst was obtained through flood modeling by incorporating a load elevation-water volume curve and the Digital Elevation Model (DEM) into the hydrodynamic model HEC-RAS. The results showed that the Kyagar glacial lake outburst was rapid and destructive, accompanied by strong currents at the end of each downstream storage ladder. A series of meteorological evaluation indicators showed that HEC-RAS reproduced the medium and low streamflow rates well. This study demonstrated the value of integrating remote sensing and hydrodynamic modeling into GLOF assessments in data-scarce regions, providing insights for disaster risk management and mitigation.

Keywords: Kyagar Glacier; Glacier lake; remote sensing; high mountain Asia; HEC-RAS

check for updates

Citation: Jiang, L.; Lin, Z.; Zhou, Z.; Luo, H.; Zheng, J.; Su, D.; Song, M. Monitoring and Disaster Assessment of Glacier Lake Outburst in High Mountains Asian Using Multi-Satellites and HEC-RAS: A Case of Kyagar in 2018. *Remote Sens.* **2024**, *16*, 4447. https://doi.org/10.3390/rs16234447

Academic Editors: Liangliang Jiang and Hailong Liu

Received: 28 October 2024
Revised: 22 November 2024
Accepted: 25 November 2024
Published: 27 November 2024

Copyright: © 2024 by the authors. Licensee MDPI, Basel, Switzerland. This article is an open access article distributed under the terms and conditions of the Creative Commons Attribution (CC BY) license (https://creativecommons.org/licenses/by/4.0/).

1. Introduction

High-latitude and mountainous regions are characterized by cold climates that have led to the formation of extensive glaciers, serving as critical freshwater sources for agriculture, domestic use, and hydropower in many countries. They serve as a critical resource for both livelihoods and economic activities, especially in arid and semi-arid regions, where the resulting oases from glacier meltwater are often the only sources of water for human settlement [1].

In recent decades, global warming (GW), driven by industrial activities, has led to significant, increasing, and extreme weather events such as heatwaves, droughts, floods, and storms. Glaciers are particularly vulnerable to GW in ecologically sensitive areas, such as high mountains. As a result of climate change, glaciers are rapidly shrinking, with significant loss of mass worldwide, which has exacerbated freshwater shortages [2].

The response of glaciers and their decline in the face of GW varies by region due to their complex terrains and regionally climatic conditions. For example, glaciers in Central Europe have experienced significant ice mass loss due to the small sizes of glaciers and insufficient snowfall replenishment; many have already disappeared in these regions, and most will disappear by the end of the 21st century [3,4]. However, glaciers in the Tibetan Plateau have exhibited diverse trends, with some regions experiencing expansion and others undergoing rapid shrinkage. In China, the amount of areas covered by glacier lakes has expanded significantly since the 1990s; glacier-fed lakes have expanded approximately six times faster than non-glacier-fed lakes. The rapid expansion of these lakes is closely tied to rising temperatures and the retreating of glaciers [5]. The Tibetan Plateau, with over 40,000 glaciers and more than 16,000 glacier lakes, has undergone dramatic changes. A total of 369 lakes have been classified as potentially dangerous based on the identification index system of glacier lake outbursts [6]. In response to GW, the surface albedo of the Tibetan Plateau had decreased over the past few decades [7,8] and increased in terms of glacier volume loss in the northern and central parts, while the southeastern regions have remained more stable or even experienced slight expansion [9]. Due to the retreating of glaciers and surging, the formation of glacier lakes plays a dual role in both the storing of freshwater and posing significant natural hazards, such as flooding, landslides, and debris flows, which have made them a critical focus of research into glacier-related hazards and disaster risk management.

Research on glacier lakes is inherently complex, as lake evolution varies by region and is influenced by timescales pertaining to glacier surging, which can range from hours to centuries. Under the influence of GW, glacier meltwater is increasingly blocked by glaciers, moraines, or bedrock, leading to the formation of glacier lakes [10]. GLOFs are sudden and catastrophic events, often triggered by glacier movement, ice dam failures, or other dynamic forces [10]. Numerous studies have investigated glacier lake outburst characteristics across various regions. In the Nyainqêntanglha Range of the Tibetan Plateau, two outburst events were analyzed using field measurements, satellite remote sensing, and hydrodynamic modeling to reveal their mechanisms and flow dynamics [11]. In the Doyinongba Basin of southeastern Tibet, remote sensing and numerical simulations were employed to study glacier lakes, showing how rapid debris influx from upstream glaciers triggered these outbursts and helped delineate hazard zones based on flood risk [12]. Given the sudden onset and destructive nature of GLOFs, these events often result in extensive loss of life and property downstream, evolving into debris flows, landslides, and other geohazards [13]. The increase in terms of the amount of glacier lakes and their size has drawn public attention to the growing risks of GLOFs since the 1990s. Populations downstream of these lakes are becoming increasingly vulnerable. On 4 October 2023, a GLOF occurred at South Lhonak Lake in the northwest of Sikkim, India, posing a severe threat to lives and property. By 5 October, at least 18 individuals had been confirmed dead, with an additional 26 injured and 102 missing, including 22 military personnel. The floodwaters also resulted in the destruction of 11 bridges [14]. Recent assessments of GLOF risks, incorporating lake conditions, exposure, and vulnerability data, have indicated that the High Mountain Asia (HMA) regions face the highest GLOF risk, while polar regions and remote areas have the lowest [14,15]. Therefore, monitoring glacier lakes in the HMA region and understanding outburst processes are critical for deepening our understanding of glacier behaviors and assessing glacier-related disaster risks.

Monitoring GLOFs in the HMA region is challenging because of the remote and high-altitude locations of glacier lakes, which make in situ observations both costly and dangerous. Moreover, the sudden nature of GLOF events, combined with the region's complex terrain, hinders data collection pertaining to the outburst process [16,17]. The rapid development of remote sensing technologies, however, has significantly enhanced GLOF research. Recent advancements in remote sensing technologies, such as the Normalized Difference Water Index (NDWI), have enabled the monitoring of glacier lake extents and dynamics [18]. For instance, the NDWI was used to track the maximum lake area of

Merzbacher Lake in the years leading up to its outburst [19]. A combination of optical remote sensing and SAR/InSAR techniques has been used to accurately monitor the spatiotemporal evolution of Jinwuco Glacier Lake in southeastern Tibet, revealing the factors that triggered its outburst [20]. However, satellite observations face limitations, including cloud cover and terrain shadows. In such cases, hydrodynamic models can complement remote sensing techniques by simulating water flow under various outburst scenarios. For example, hydrodynamic modeling was used to assess the impact of the Galong Co Glacier Lake outburst in downstream regions, demonstrating how deeper breach depths lead to greater downstream impacts [21]. Additionally, a combination of 1D and 2D hydrodynamic modeling was used to assess the flood risk posed by the potential outburst of Satopanth Lake in the central Himalayas [22]. Combining remote sensing data with hydrodynamic modeling offers a comprehensive approach to studying GLOFs. Remote sensing provides valuable input parameters for hydrodynamic models, ensuring that the simulated flood dynamics align with actual observations. This integrated approach enables high-resolution assessments of GLOF events, supporting disaster risk reduction in the HMA region. The Kyagar Glacier is a notable example of a glacier with a history of frequent outburst floods. Between 1961 and 2021, the Kyagar Glacier lake experienced 30 outburst floods, with August being the most common month for such events, followed by July [23]. One particularly notable event occurred on 4 September 1961, when a GLOF destroyed a bridge on the Yarkant River, causing direct economic losses of 1 million yuan. Outburst floods in 1982 and 1984 caused significant damage to downstream infrastructure, including the Karqun diversion project [24].

Numerous studies have concentrated on utilizing remote sensing data to investigate the Kyagar Glacier surge and the hazard resulting from the breach of the ice tongue; however, there is a paucity of scholarly work that conducts dynamic analyses of inundation events in the downstream areas. By matching model simulations with real-world observations under different flow scenarios, this research aims to contribute to the assessment of GLOF hazards and provide a method for estimating flood discharge in areas where flow monitoring stations are difficult to establish. Section 2 describes the study area, data sources, core methodologies, and operational techniques, with a particular emphasis on depth extraction methods based on satellite data. Additionally, this section outlines the fundamental principles and specific parameter settings employed in GLOF modeling. Section 3.1 presents the water depth data obtained through direct inversion using remote sensing data, establishing a foundational dataset for the GLOF hydrodynamic model. Section 3.2 illustrates the hydrodynamic model's representation of the GLOF event, examines the hazard characteristics revealed by this model, and provides an evaluation based on remote sensing data. Chapter 4 discusses the study's limitations and considers future applications in hazard assessment, disaster prevention, and early warning systems for glacial lake outbursts. Finally, Chapter 5 summarizes the key findings of this study.

2. Materials and Methodology

2.1. Study Site

Kyagar Glacier is located on the northern slopes of the Karakoram Range and next to Shaksgam Valley, playing a significant role in the Yarkant River's flow path [25]. Due to its high altitude and cold climate, this area is ideal for glacier formation and movement. The slow northward movement of the Kyagar Glacier results in the accumulation of an ice tongue on its northeastern side within the Shaksgam Valley [26]. This ice tongue, with a height ranging from 50 to 150 m and a width of about 1.5 km, plays the role of a reservoir dam and blocks the valley's riverbed, forming a glacier lake with a storage capacity exceeding 230 MCM (million cubic meters) [27].

The coordinates of the glacier lake are approximately 35.67°–35.68°N and 77.17°–77.22°E (Figure 1a). The glacier tongue extends 8 km, with a width of 1.5 km. The tongue surface is rugged, with a significant spatial span and an average slope of more than 2°. These factors contribute to the formation of a natural ice dam that blocks the valley's riverbed and

enables the accumulation of water on the eastern side of the glacier tongue [25,28]. During non-outburst periods, the ice tongue acts as a partial barrier. The glacier's complex system of crevasses and fluvial channels, located under the northern side of the ice tongue, acts as a drainage pathway, connecting the glacier lake to the downstream Keleqin River [28]. When the hydrological pressure in these crevasses reaches its peak, large-scale drainage events occur, which were the primary mechanism behind outburst events before 2017 [26]. After 2017, the increased mass of the Kyagar Glacier tongue enhanced its blocking ability, resulting in the 5th highest of all records of WSE in 2018 of the Kyagar Glacier lake [29]. The thickening of the ice tongue overwhelmed existing drainage channels, causing them to close. Meanwhile, erosion on the northern side of the ice tongue created a stable flow channel, which became one of the primary drainage pathways during the 2018 outburst [26].

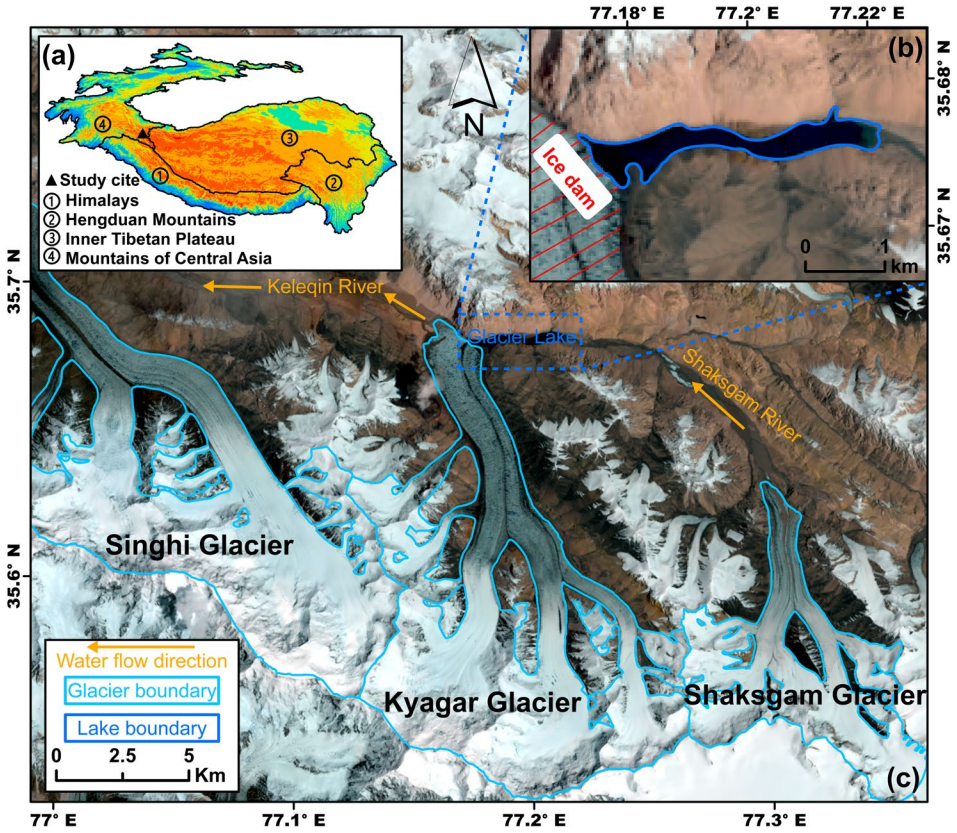


Figure 1. Kyagar Glacier lake. (**a**) The location of the lake in the HMA region. The black triangle represents the Kyagar Glacier. The background was made with DEM using the Shuttle Radar Topography Mission (SRTM) and HMA boundary [30]. (**b**,**c**) Geographic location of the Kyagar Glacier and lake. The image is a false-color composite based on Landsat 8 Level-2 surface reflectance data acquired on 12 July 2018, using bands 5, 4, and 3. The glacier boundary data were from the National Tibetan Plateau/Third Pole Environment Data Center. https://cstr.cn/18406.11.glacier.001.2013.db (accessed on 26 October 2024) [31,32].

2.2. Datasets

This study used a combination of tools, including Google Earth Engine (GEE, https://code.earthengine.google.com/ (accessed on 26 October 2024) and the Sentinel Application Platform (SNAP), to process the Sentinel-1 (S1) and Sentinel-2 (S2) satellite data. These data were used to extract the water masks and calculate lake volume and streamflow. The HEC-RAS model was then employed to simulate the event. The flowchart (Figure 2) illustrates the process of obtaining and analyzing remote sensing data, as well as the steps for hydrodynamic modeling.

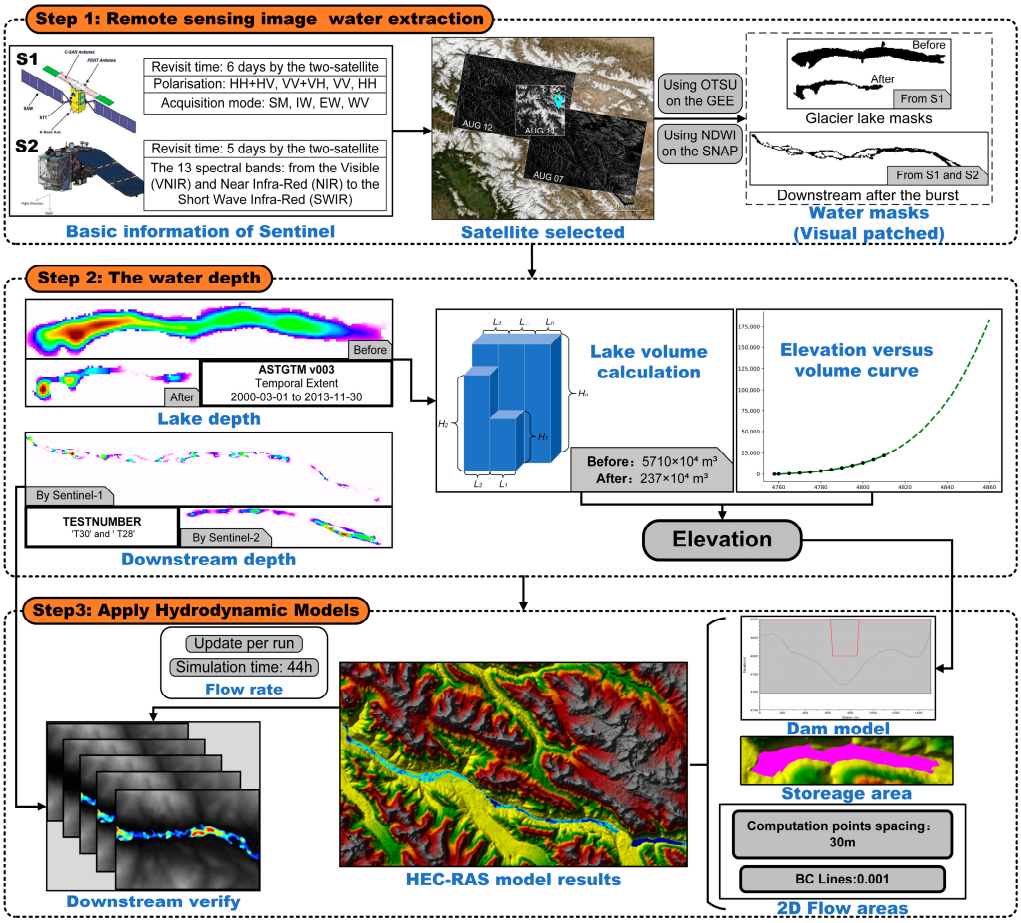


Figure 2. Flowchart of data processing of remote sensing and hydrodynamic modeling process. The satellite parameters information was from Sentinel Online-SentiWiki (https://sentiwiki.copernicus.eu/web/s1-mission (accessed on 25 September 2024). S1 and S2 images credits: TAS-I and EADS Astrium.

We focused on the Kyagar Glacier outburst event that occurred on 10 August 2018, drawing from the GLOF inventory for the High Mountain Asia (HMA) region. For data collection, we used satellite data collected before and after the event, including Sentinel-1 and Sentinel-2 data from 7 August to 12 August 2018. The S1 dataset used in the GEE is represented by COPERNICUS/S1_GRD, which includes Ground Range Detected (GRD) scenes processed through the Sentinel-1 Toolbox to yield calibrated, ortho-rectified products. For this study, we selected the Interferometric Wide (IW) swath acquisition mode and dual polarization (HH&HV) configurations [33]. S2 data were sourced from a wide-swath, high-resolution, multispectral imaging mission. To streamline the workflow, we used Sentinel-2 Level-2A (L2A) products, which were ortho-rectified and provided Bottom-of-Atmosphere (BOA) reflectance [34]. Digital Elevation Model (DEM) data were acquired from the Advanced Spaceborne Thermal Emission and Reflection Radiometer Global Digital Elevation Model V3 (ASTGTM v003), jointly developed by NASA and the Japan Aerospace Exploration Agency (JAXA), covering the region from 35°N to 36°N and 76°E to 77°E. In preliminary tests, alternative DEM datasets, including ALOS (12.5 m), SRTM30M, and NASADEM (30 m), were assessed. However, the selected DEM proved to be the most suitable, as other datasets failed to accurately represent water depth. These inaccuracies were largely due to extensive downstream data gaps and, in some instances, inconsistent glacier water depth patterns relative to the DEM data, occasionally even producing inverse depth representations.

2.3. Approach of GLOF Detection in Sparse Observation Region

2.3.1. Water Mask Derived from Remote Sensing Images

This study utilized data provided by the European Space Agency's (ESA) Sentinel-1 and Sentinel-2 satellites (Figure 2). Sentinel-1, equipped with a Synthetic Aperture Radar (SAR), was chosen for its capability to penetrate cloud cover and provide reliable observations in poor weather conditions, as well as its frequent revisit periods. Dual-polarization datasets from 7 August and 12 August were processed using Google Earth Engine (GEE), a platform developed in collaboration with Google, Carnegie Mellon University, and the United States Geological Survey (USGS), to extract water bodies from glacier lake images and downstream water features using OTSU-based hydrological extraction methods [35]. Sentinel-2 data were processed using SNAP V11.00 software. The Normalized Difference Water Index (NDWI), derived from surface reflectance data of bands 3 and 8, was used to extract water bodies [36]. This index effectively reduces interference from vegetation and soil, proving particularly successful in extracting large lake reservoirs [37]. Results with an NDWI value greater than 0 were selected, and visual corrections were applied using ArcGIS V10.2 to refine the extracted water body data (Figure 2).

2.3.2. Water Depth Estimation

The FwDET calculates water depth by subtracting the topographic elevation of each grid cell within the flooded area from the flood surface elevation (above mean sea level, a.m.s.l.) derived from a DEM [38]. The core of the FwDET algorithm is the identification and application of the elevation of the boundary between water and land. The algorithm procedure [39] is as follows: (1) converting the water mask to a line layer, which is the boundary of water; (2) identifying from the boundary the grid cells that are the same size as the DEM; (3) extracting the elevation values from the DEM for these grid cells at same location (referred to as boundary grid cells elevation, BCE); (4) assigning the BCE to each grid cell within the flood domain from their nearest grid cells; and (5) calculating water depth by subtracting the elevation of DEM from BCE at each grid cell, as shown in Figure 3.

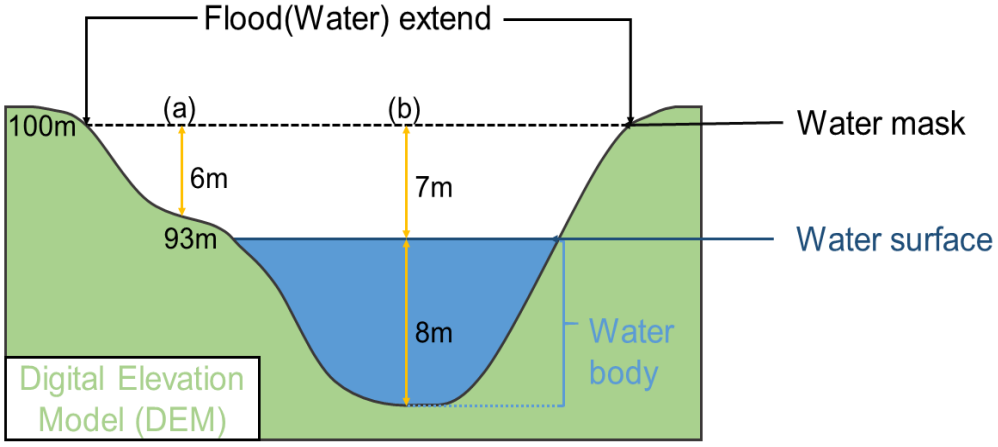


Figure 3. This is a cross-section diagram illustrating the principle of the FwDET calculation of flood depth. For example, if the imported water mask has an elevation of 100 m, the tool computes the water depth below each grid cell within that mask. In perennial rivers, the calculated depth tends to be underestimated, as measuring instruments for satellites usually capture the WSE rather than the riverbed, resulting in a reference plane for DEMs at the water surface. The point of (a) and (b) is separately land and waterbody in none flooding time. The actual water depth at point (a) and (b) is 6 m and 15 m, respectively.

FwDET v2.1 introduces a boundary grid-smoothing and filtering process, using a box 5 × 5 grid for boundary elevation smoothing and multiple iteration loops to refine outputs [40–42]. In FwDET, both the extracted water body imagery and the selected DEM are crucial inputs, as well as specific settings for the Slope Filter (SF) and Iterations Option

(IO). Inputting appropriate SF and IO can repair the sharp transition area and streak area in the output result to a certain extent.

Custom parameter configurations (T01 to T31), those developed by the algorithm's owner and consisting of various SF and IO combinations, were tested iteratively (Table 1). "CustoNumber" (CtN) refers to customizable parameter sets, which were used to compare different presets. This study integrates the extracted water masks with 30-m resolution ASTER GDEM data and applies the FwDET v2.1 to obtain optimized depth results for both lakes and downstream rivers (see Step 2 in Figure 2). By multiplying each pixel's depth with its corresponding resolution and summing the resulting values across all pixels, the lake volumes before and after the outburst were calculated. The difference between the before and after outburst lake volumes, divided by the time elapsed between satellite image captures, yielded an estimated average outburst discharge.

Table 1. Different combinations of slope filter and iterations option.

CtN	SF	IO	CtN	SF	IO	CtN	SF	IO
T01	0.5	1	T11	1.5	1	T21	2.5	1
T02	0.5	2	T12	1.5	2	T22	2.5	2
T03	0.5	3	T13	1.5	3	T23	2.5	3
T04	0.5	4	T14	1.5	4	T24	2.5	4
T05	0.5	5	T15	1.5	5	T25	2.5	5
T06	1.0	1	T16	2.0	1	T26	FALSE	1
T07	1.0	2	T17	2.0	2	T27	FALSE	2
T08	1.0	3	T18	2.0	3	T28	FALSE	3
T09	1.0	4	T19	2.0	4	T29	FALSE	4
T10	1.0	5	T20	2.0	5	T30	FALSE	5
						T31	FALSE	FALSE

2.3.3. GLOF Modeling with HEC-RAS

The Hydrologic Engineering Centers River Analysis System (HEC-RAS), developed by the US Army Corps of Engineers, is widely used for river hydrology and hydraulic modeling. It supports two-dimensional hydrodynamic analysis by solving either the full Saint-Venant equations or the simplified 2D diffusion wave equations. HEC-RAS has been extensively applied in the hazard assessment of GLOFs in steep terrains, such as the Himalayas, offering a promising approach for regional simulations of dam-break scenarios [22,43]. For this study, three key elements were modeled: Storage Area (SA), SA/2D Connections, and the 2D Flow Area (Step 3 in Figure 2).

First of all, the glacial lake upstream of the dam was modeled as a storage area, replacing the reservoir's function. We achieved quantitative control over the storage area by inputting 100 numerical points of the elevation-water volume curve. The initiation and termination of the outburst event could be regulated by adjusting the WSE at the onset and cessation of the breach taken from the remote sensing data. Due to the lack of field observations in the study area, empirical equations were used to estimate the flood hydrograph and breach development, which provided upstream boundary conditions for the storage area.

Secondly, the dam was modeled as SA/2D Connections by us, which represented the breach development during the outburst. Natural dam breaches often have complex, hard-to-measure shapes, being triangular, trapezoidal, or rectangular. Based on prior observations, this study used a trapezoidal shape [44]. Empirical equations were applied to estimate two key breach parameters: the average breach width (B_{ave}) and breach development time (T_f). As a result of considerations for minimizing the input of uncertain parameters, this study opted to employ the Von Thun and Gillette equation [45].

$$B_{ave} = 2.5h_w + C_b \quad (1)$$

$$\begin{cases} T_f = \frac{B_{ave}}{4h_w} (Erosion\ resistant) \\ T_f = \frac{B_{ave}}{4h_w + 61.0} (Prone\ to\ erosion) \end{cases} \quad (2)$$

where h_w is lake depth above the bottom of breach (m), C_b is a coefficient, which is a function of reservoir size (Table 2).

Table 2. Values of C_b are based on reservoir size.

Reservoir Size (m^3)	C_b (m)
$<1.23 \times 10^6$	6.1
1.23×10^6–6.17×10^6	18.3
6.17×10^6–1.23×10^7	42.7
$>1.23 \times 10^7$	54.9

The development time of the breach was calculated using Equation (2) using the estimated average breach width. It is worth noting that the breach development time equation differentiates between dams made of "erosion-resistant" and "erosion-prone" materials. In the study by Von Thun and Gillette, it was recommended to consider well-structured, erosion-resistant dams as the upper bound and poorly structured, easily erodible dams as the lower limitation of the calculations, respectively. The triggering mechanism for a dam breach was considered as overtopping. The computational results indicated that the width of the breach at the base was approximately 135 m, with side slopes of the trapezoidal breach at 0.5, and the breach formation time was around 1.05 h.

Finally, a 2D flow area was defined downstream of the dam, extending from the dam to 92,279.5 m and was subdivided into grids of equal size at 30 × 30 m. Then, we computed 2D flow area hydraulic tables to preprocess the 2D flow area's computational cells and faces into detailed tables based on the underlying terrain data to make sure the 2D hydrodynamic calculations were performed for each scenario. The total simulation time was 44 h, including a computation interval of 10 s and mapping output intervals set to 1 min. Four Boundary Condition Lines (BC Lines) were artificially set along the downstream segment to guide the flow in the correct east-west direction with a friction slope (S_f in Manning's formula [46]; the slope of the energy grade line) of 0.001 applied to the downstream boundary conditions.

$$Q = VA = \left(\frac{1}{n}\right) AR^{\frac{2}{3}} \sqrt{S_f} \quad (3)$$

where Q is the flow rate (m^3/s), V is velocity (m/s), A is the flow area (m^2), n is Mannning's Roughness Coefficient, and R is hydraulic radius (m).

2.4. Evaluation Metrics

In the field of numerical weather forecasting, prediction methods for precipitation primarily rely on satellite cloud imagery and radar echo extrapolation. The objective evaluation of forecast products is a crucial step in the operational workflow. Some widely used metrics have been utilized to evaluate the performance of radar-estimated rainfall and severe precipitation events [47–49], such as the Threat Score (TS), also known as the Critical Success Index (CSI), the False Alarm Ratio (FAR), and the Probability of Detection (POD) [50].

$$\mathrm{TS} = \frac{\mathrm{TP}}{\mathrm{TP} + \mathrm{FP} + \mathrm{FN}} \times 100\% \quad (4)$$

$$\mathrm{POD} = \frac{\mathrm{TP}}{\mathrm{TP} + \mathrm{FP}} \times 100\% \quad (5)$$

$$\mathrm{FAR} = \frac{\mathrm{FP}}{\mathrm{TP} + \mathrm{FP}} \times 100\% \quad (6)$$

where refers to the number of correctly predicted grid (or station) points, FP represents the number of false alarms, FN denotes missed forecasts, and TN indicates correctly predicted non-rainy points, as defined in the contingency table in Table 3. The waterbody is defined as the region with a water depth greater than 0.1 m in HEC-RAS simulations and detected as water from satellite images. TS measures the ratio of correct water cover in the simulation of HEC-RAS (successes) against observations of the water mask identified through remote sensing (including false alarms and missed events). POD reflects the proportion of true positives among the predicted positives, with higher POD values indicating a higher probability of correct simulation and thus greater reliability. FAR, on the other hand, measures the ratio of false positives to all simulated samples.

Table 3. Confusion matrix of rainfall classification.

		Is Waterbody in Simulated Output of HEC-RAS	
		True	False
Is waterbody in observation of satellite images	True	TP (True Positive)	FP (False Positive)
	False	FN (False Negative)	TN (True Negative)

3. Results

3.1. Depth and Flow Estimation from Multiple Remote Sensing

3.1.1. Changes in Upstream Glacier Lake

Though previous studies have recommended 10 iterations and a 0.5% slope threshold as generally effective for most DEMs, these settings were suboptimal for our calculations [40].

We assumed that the WSE of the lake was consistent throughout and drew three polylines named Profile A-Profile C covering the east and west sides of the lake (Figure 4). The values of water depth and terrain along these polylines were then extracted. Under the assumption of a uniform WSE, the rates of change in water depth along the polylines were expected to be inversely proportional to the rates of change in terrain. We calculated the percentage of instances where these changes were inversely related, with a higher percentage indicating a more accurate representation of the lake's calculations; otherwise, it was the opposite. In this study, we analyzed the two sets of inversion results before and after the lake outburst and calculated the inversely related percentage along six selected polylines (Figure 5). In the before scenario, it can be observed that the calculations for T28–T30 show better agreement, with the calculated lake area closely matching the results of water body extraction. In the after scenario, Profile C stands out as the primary polyline with a higher proportion of opposite slopes and less fluctuation, showing relative consistency and a higher success rate for T24–T30 when compared to the other two profiles. Based on these findings, the results from T30 and T28 were selected to represent the lake depths before and after the glacier lake outburst in the subsequent sections.

Before the outburst, the glacier lake expanded due to glacial meltwater and rainfall, reaching a surface area of 2.25 km^2 and a capacity of 57.10 MCM, slightly below the 2017 record. The before outburst imagery (Figure 4a) shows deeper areas close to the dam, with depth decreasing from west to east. This configuration channels water from the Shaksgam Valley to the lake, priming the lake for a rapid and violent outburst. At this stage, the maximum water depth was 61.78 m, with an average depth of 27.01 m. In the early morning of August 10, a large amount of lake water gushed out through the dam, but due to the limited water level and the flow channel, the lake could not completely pour out. Following the outburst (Figure 4b), only minimal residual water remained, with a maximum depth of just 15.08 m and an average depth of 5.90 m.

With this depth data, the total lake volume was computed by summing the products of the pixel depth and the pixel area, obtaining an estimated mean discharge rate of 126.6 m^3/s over 432,476 s.

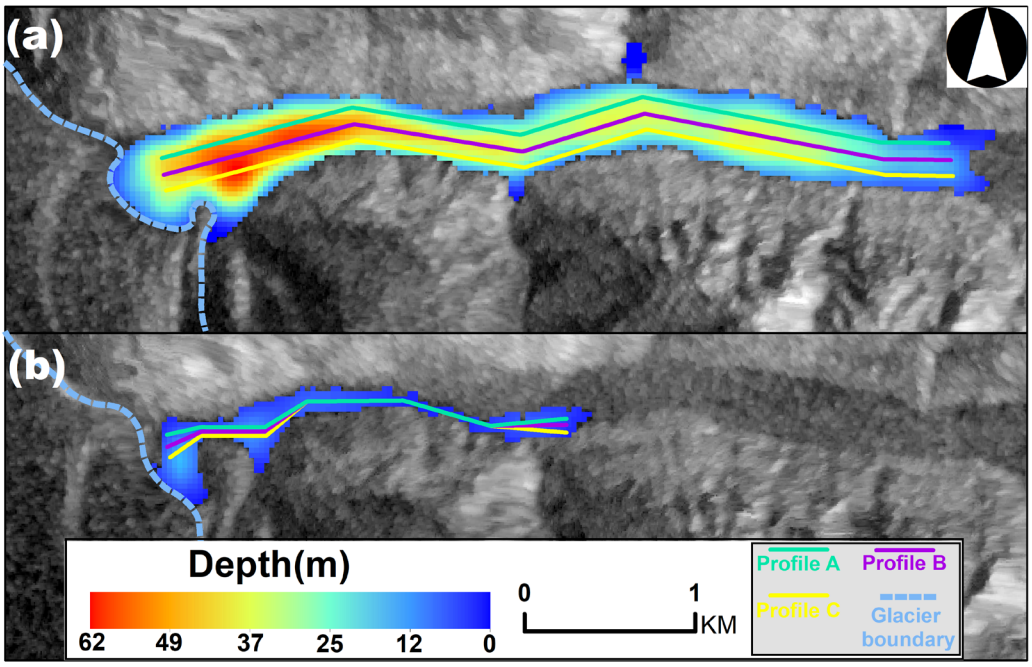


Figure 4. FwDET-generated water depth maps for the Kyagar Glacier lake. Background: Sentinel-1 dual-polarization images acquired on 7 August (before outburst) and 12 August (after outburst), 2018. (**a**) Before the outburst on 7 August 2018 by Sentinel-1. (**b**) After the outburst on 12 August 2018 by Sentinel-1.

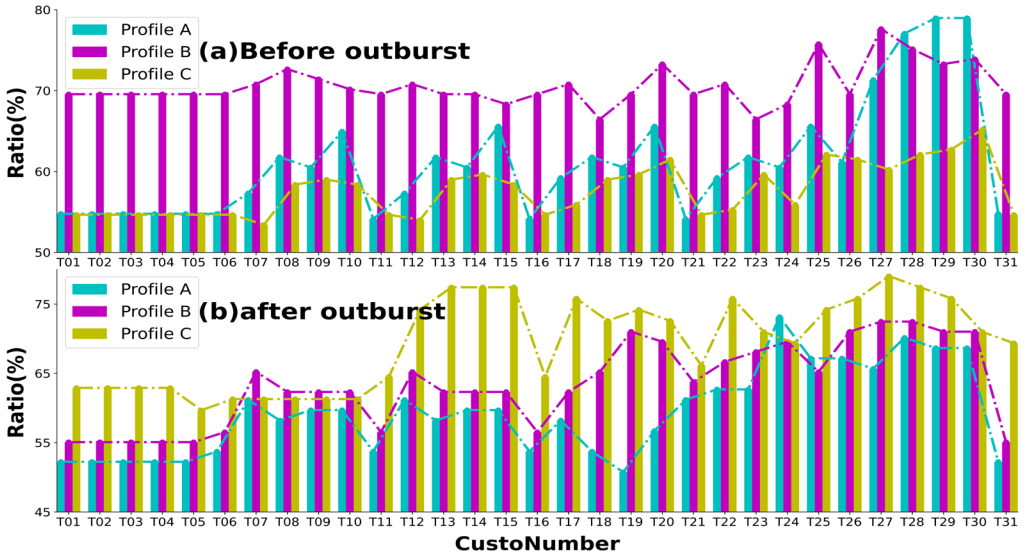


Figure 5. Slope filter and iteration setting combinations in FwDET and their respective success rates for computation results.

3.1.2. Downstream Flooding Process

Downstream of the glacier is different from the lake, resulting in difficulty and inauthenticity for the FwDET inversion of the downstream. In this section, we calculated the percentage of the water flow area obtained from inversion results under varying parameter conditions relative to the water mask abstracts (visual patches) from the remote sensing data (Step 1 in Figure 2). According to the success count ratio (Figure 6), for T1–T25, the success rate of 12 August remained below 35%, while 11 August showed a maximum success rate of approximately 60% and a minimum of 23%. However, when the parameter combinations reached T26–T30, the success rate rose sharply, with the average success rate for both the 11 August and 12 August exceeding 70%. This indicates that inversion results are more

reliable with larger parameter combinations. Accordingly, this study utilized the depth results calculated under the T30 combination as reference data for subsequent analyses.

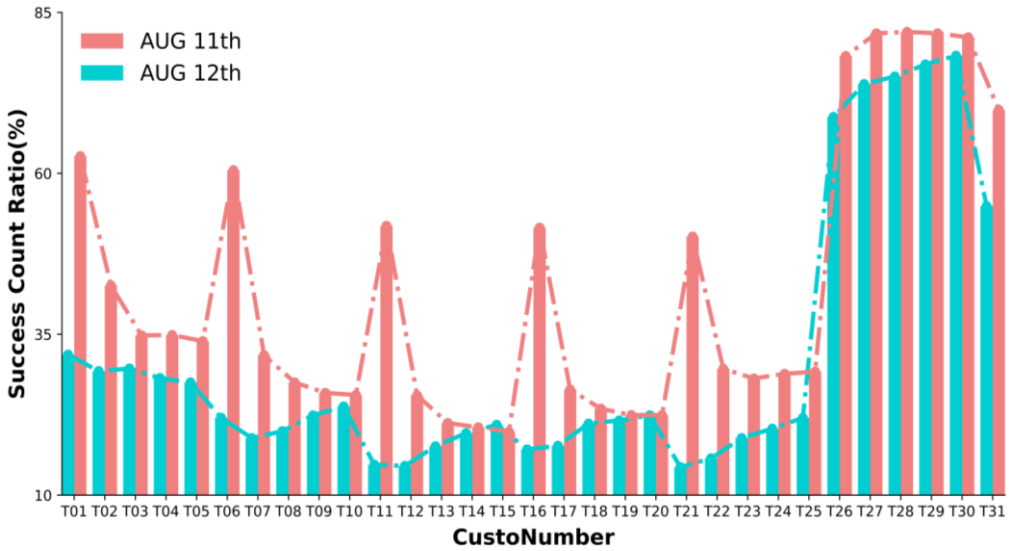


Figure 6. Area percentage of FwDET-derived results under varied parameter combinations, based on Sentinel-2 (11 August) and Sentinel-1 (12 August) data for downstream rivers that were abstracted.

Based on the depth maps of the downstream after the outburst (Figure 7) and remote sensing data, several key observations can be made. First, the downstream region exhibits an overall west-to-east decrease in elevation, a feature that prevents backflow from the lake during discharge events. Second, there is a substantial elevation drop between the dam crest and downstream areas, with a height difference exceeding 50 m. This significant drop in height facilitates the rapid discharge of lake water during dam breach events, leading to intensified flood flows. Lastly, the downstream river network is complex, with segments that become disconnected during periods outside the peak flood. These characteristics are evident for 12 August (Figure 7b), where the peak discharge phase has already passed, resulting in markedly reduced flow, consequently creating a sparse and shallow river network near the glacier tongue.

3.1.3. Elevation-Water Volume Curve

Building on the lake depth data obtained from the water masks, we calculated the lake volume to estimate the average discharge rate. Beyond direct discharge calculation, the lake volume also enables us to derive corresponding WSEs, achieved by constructing a storage capacity curve. This curve represents the relationship between the WSE (x-axis) and the lake volume (y-axis). In previous research, the lake area and volume at different elevations were estimated by using contour analysis and a parabolic fitting method based on GIS lake outlines and a recent DEM [51]. In this study, we extended these findings by interpolating 12 elevation-volume data points using Python V3.11. To ensure the extrapolated curve encompassed lake volumes before and after the outburst, we generated 1000 points uniformly between 4758 m and 4860 m and applied cubic spline interpolation to create a continuous, smooth curve. This approach maintained consistent trends in the curve for x-values above and below 4810 m, ensuring continuity in volume estimations.

The elevation-water volume (Figure 8) indicates that the volume of the lake before the outburst was approximately 57.1 MCM at a WSE of 4830.2 m, and the volume of the lake after the outburst was approximately 2.4 MCM at a WSE of 4774.7 m, closely aligning with the mean values derived from combined depth and DEM data, for which the WSE before the burst was 4830.1 m, while after it was 4784.8 m. The error between the inversion result and the storage capacity curve after the collapse was 0.2%. Thus, we obtained the elevation-water volume curve and WSEs for both before and after the outburst.

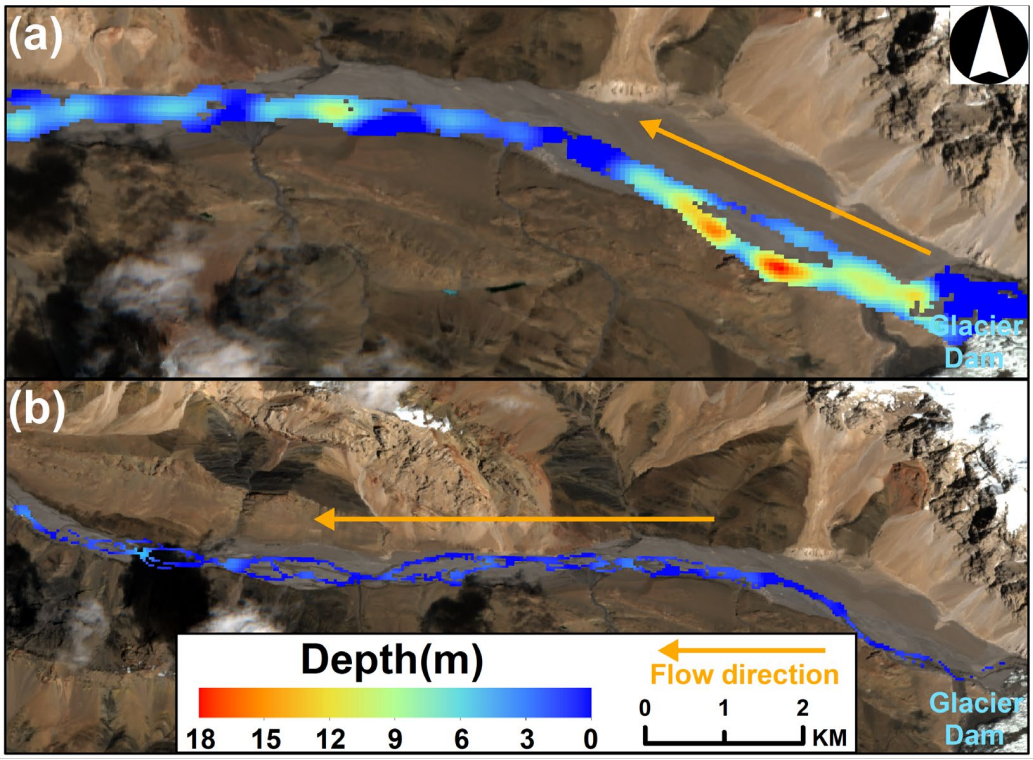


Figure 7. FwDET-generated water depth maps for the downstream after the Kyagar Glacier lake outburst. Background: True-color composite image of Sentinel-2 satellite data based on B4, B3, and B2 bands. (**a**) Represents 11 August 2018 by Sentinel-2. (**b**) Represents 12 August 2018 by Sentinel-1.

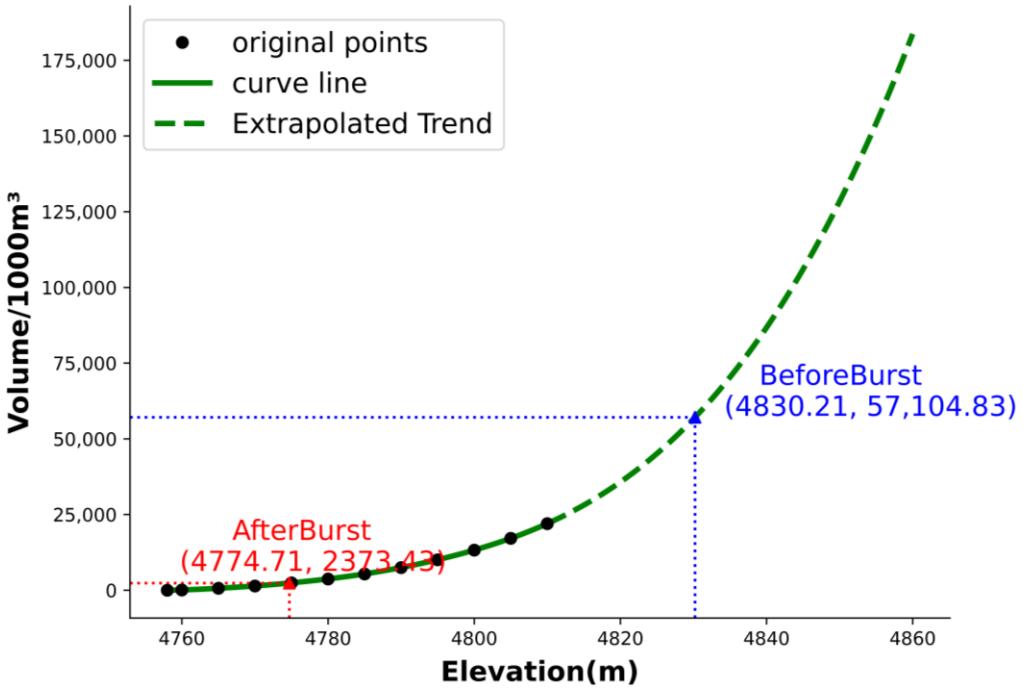


Figure 8. Elevation-water volume curve for the lake derived via interpolation.

In fact, due to the distinctive structure of the Kyagar glacier dam, which is a mix of permafrost and ice layers rather than a tightly sealed dam, the lake undergoes continuous drainage even outside breach events, especially when nearing the dam's maximum holding capacity. This causes a gradual movement in the lake water from east to west, flowing from

high to low areas. Consequently, the WSE across the lake is not uniformly distributed but varies spatially. The WSE is an average value.

3.2. GLOF Process Modeling by HEC-RAS

3.2.1. Hydrograph Modeling

To accurately estimate downstream flooding, precise estimates of the breach location, size, and development time are essential, though these parameters often introduce substantial uncertainty in the analysis. Due to limited field observations, this study utilized regression equations of HEC-RAS for breach modeling, built by Von Thun and Gillette [45]. To simulate the storage area in the model, we randomly selected 100 points within the 4748–4860 m range from the elevation-water volume curve. Given the complex structure of the glacier dam and Kyagar Glacier's surge mechanism, we set the final bottom elevation of the breach to 4800 m, which was 0.3% higher than the WSE from the combination of depth and DEM. This higher-than-average WSE made sure the water was directed downstream while facilitating breach progression. This adjustment ensured the simulated outcomes were similar to the after-outburst imagery attained through remote sensing (Figure 4b).

Figure 9 illustrates the model-simulated lake coverage area and water depth. A few outlier regions with unreasonable extreme water presence were excluded from the analysis. In Figure 9a, the before-outburst lake area, which was simulated by the HEC-RAS model based on the elevation-water volume curve, closely matches the before-breach lake area (Figure 4a) derived from remote sensing data. Moreover, from the perspective of depth observation, both demonstrate a similar pattern in terms of greater depth in the west and shallower waters in the east. Following the burst, the lake area rapidly decreased, with a corresponding sharp decline in WSE, continuing until approximately 0900 am on 10 August 2018. During the simulation, it was evident that, by the third hour, lake dynamics began to stabilize, with only minor fluctuations in lake area and water volume. As observed in Figure 9j, during the model's final equilibrium phase, the simulated lake area was slightly more than the lake area gained from remote sensing data (Figure 4b).

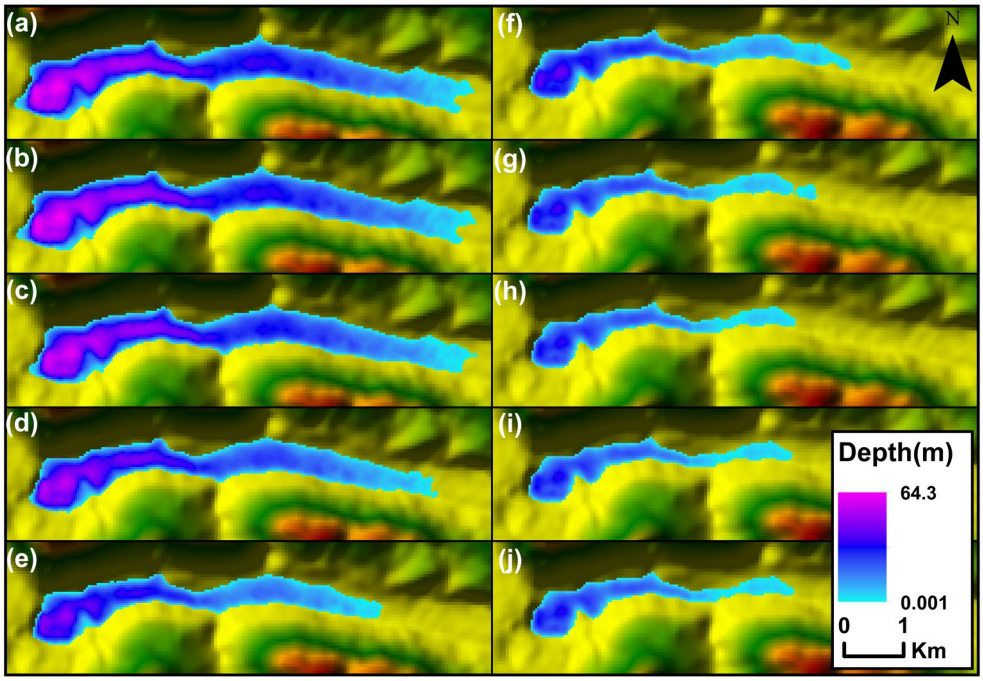


Figure 9. Images of glacier lake evolution over time as simulated by HEC-RAS. (**a**–**e**) The lake image times on 10 August 2018 at 6:00 a.m., 6:10 a.m., 6:20 a.m., 6:30 a.m., and 6:45 a.m. (**f**–**j**) The lake image times on 10 August 2018 at 7:00 a.m., 7:30 a.m., 8:00 a.m., 8:30 a.m., and 9:00 a.m.

The outburst process of the Kyagar Glacier lake involved the rapid discharge of a substantial water volume. Profiles revealed a stepped structure in the downstream flow path: 0–5314 m as the first step, 5314–10,203 m as the second step, and 10,203–14,852 m as the third step. During the outburst, the rapid flow along each step initiated abrupt increases in velocity, with water accumulating until it reached the elevation of the next step. In the first step of water storage, the velocity was relatively high when the flow initially entered, causing the rapid rise in WSE (Figure 10a–c). However, during the subsequent process of water delivery, the velocity gradually decelerated until it reached a stable WSE. The second and third steps had higher drops and more turbulent water flows compared to the first step, and there existed a rough terrain section of riverbed. The main water storage areas of the second and third steps were still located at the end of each step, while the areas with the highest velocities were the rough riverbed areas. For each step, when the water storage exceeded the bearing capacity of the step, due to the drainage effect, the water storage height of the step gradually decreased until it was eventually level with the terrain that divided the steps.

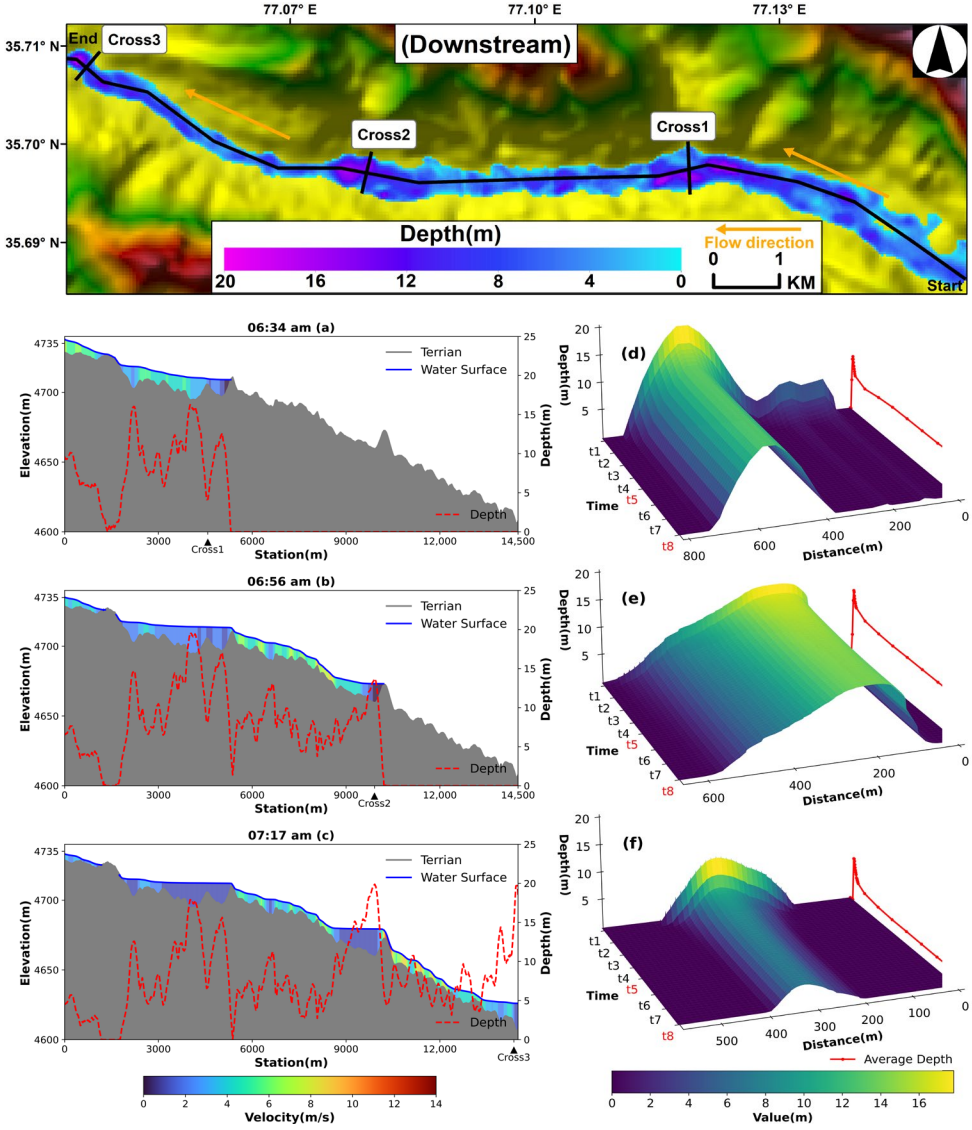


Figure 10. Inundation maps for downstream regions of the glacier dam over time, as simulated by HEC-RAS. The inundation diagram from HEC-RAS, which is a union of the maximum inundation depths in each part during modeling. Start-end indicates the longitudinal line of the downstream river taken along the flow direction. (**a**–**c**) The results of the outburst model transform with time and

distance along the start-end, while cross1-3 represent the locations where three-dimensional views of water depth change over time at different cross-sections. (**d**–**f**) The variations of water depth along the cross1–3 with time at different points. Each time interval (t1–t8) represents a snapshot within the overall simulation, with t5 (11 August 5:36 a.m.) and t8 (12 August 0:58 a.m.) matching satellite data acquisition times. The average depth represents the average rate of water depth on the crosses.

To investigate depth variations across main storage areas in each step, we constructed three cross-sectional profiles nearly perpendicular to the start-end line. We created a 3D visual map of water depth changes over time from the cross-sections. These panels (Figure 10) revealed that the river is widest in the first step, with an average width of 670 m (Figure 10d), and average widths of 610 m (Figure 10e) and 200 m (Figure 10f) in the second and third steps, respectively. At the end of the first step and the beginning of the second, uneven terrain results in a complex water network with multiple maxima. This effect, caused by extended low-lying areas downstream of the glacier tongue, enhances water storage and flow during non-outburst events and serves as a stable conduit. The confinement of water to these lowlands under simulated outburst conditions leads to prolonged retention in specific grid cells due to limited model resolution, creating regions of slower flow and even potentially permanent standing water.

3.2.2. Optimal Parameters Assessment

To evaluate the accuracy of the simulated inundation depths compared to the actual flood data, a binary threshold of 0.1 m was used to distinguish flooded from non-flooded areas. Meteorological scoring functions were introduced: POD represents the proportion of correctly predicted flooded areas relative to the total actual flooded areas, CSI reflects the ratio of correctly predicted flooded areas to the total number of predicted and observed flooded areas, and FAR quantifies the percentage of false alarms, or areas incorrectly predicted as flooded [47,50].

3.2.3. Evaluation Against Remote Sensing

In Figure 11, the evaluation metrics reveal that POD and CSI generally increase as flow rates approach 130 m^3/s, indicating the model's reliability within moderate flow scenarios. Beyond 130 m^3/s, the changes in metric values stabilize. Initial increases in POD and CSI were due to the low discharge flow, which limited the spread and extent of inundation within the simulation timeframe, resulting in higher omission rates. With the rising of the streamflow, the modeling outcomes improved in matching observed width and extent, enhancing hit rates. At higher streamflow, modeling outcome performance stabilized for two reasons: (1) The inundation simulation area corresponds with available remote sensing data, which are limited to portions of the river, constraining excessive false alarms. Increasing discharge causes water to flow further downstream, restricting its interaction with comparable satellite observations. (2) Downstream water-holding capacity limits further accumulation within the model's domain (Figure 10), requiring water to spread laterally. Comparing the model results for 11 and 12 August at lower flow rates suggests a better model fit to 11 August data, which represent the immediate after-outburst period. The rapid flow in the early stages of the outburst explains the wider and deeper river observed in the 11 August satellite image, correlating closely with simulated conditions around 5:36 am on 11 August. Consequently, the model achieves higher POD and CSI, with lower FAR on this date.

Overall, we conclude that the Kyagar Glacier lake outburst model is best suited for moderate flow rates, with an upper limit near 132 m^3/s. The estimated average discharge rate of 126.6 m^3/s calculated from before and after outburst lake capacities is thus considered reliable. This model is less suitable for extreme flood events, as indicated by historical data showing that, out of 20 outbursts from 1959 to 2020, 8 exceeded 130 m^3/s, with peak flows reaching up to 6000 m^3/s [23,52].

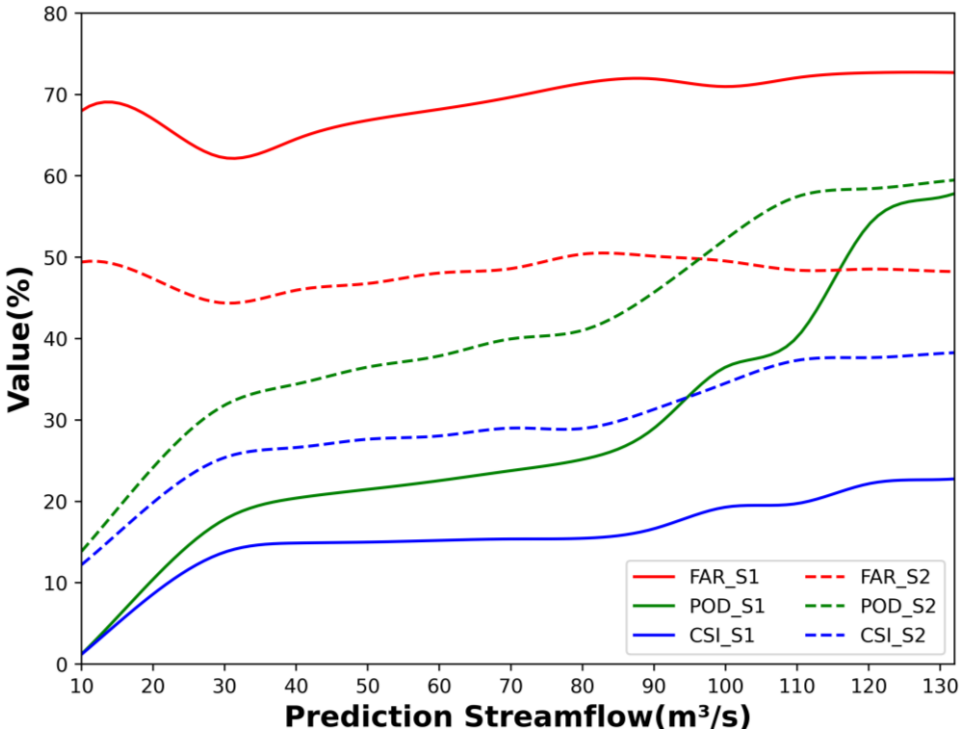


Figure 11. Model evaluation based on POD, CSI, and FAR metrics across varying average flow rates. S1 represents downstream depth inversions using FwDET based on Sentinel-1 imagery (12 August), while S2 reflects Sentinel-2 data (11 August). We excluded the results where the flow rate was greater than 132 m^3/s. This is because an overly large average flow rate would exceed the total water capacity of this glacier lake.

4. Discussions

The burst of this particular glacier dam occurred in the early morning of 10 August 2018. We used the satellite data obtained on 7 August 2018 as a reference for the lake image before the outburst. Due to the lack of data, we could not determine how different the lake image (Figure 4a) extracted on August 7 was from the real lake. Therefore, the conclusion of this article is based to a certain extent on the hypothesis that the lake surface did not change until the burst event. The water extent extracted from S1 data has limitations. However, with the gradual development of machine learning, the use of optical sensing satellites with higher revisit rates for water mask extraction has made it possible to obtain better lake images [53]. This would be an approach worth considering for other GLOFs.

This study utilized satellite data from various sources to monitor and characterize glacial lake structures, a foundational step for effective GLOF analysis. However, the rapid outburst of the Kyagar Glacier lake and the swift downstream flow presented challenges in capturing detailed observations through satellite imagery. The Kyagar Glacier lake exhibits a distinct cyclical filling-and-bursting pattern, with similar outburst events. This study focused on a single case of such an event; however, due to the cyclic nature of these disasters, multiple cases are often necessary to substantiate experimental results, highlighting a limitation of the study's generalizability.

Extracting accurate hydrological images from satellite data remains challenging, as the automated recognition of water bodies can underestimate their actual extent. The Kyagar Glacier lake formed due to the Kyagar Glacier's ice tongue, which facilitates water accumulation. Complex glacier surging behaviors and physical mechanisms can result in ice mixed with sediment near the water surface. This mixture reduces SAR signal reflectance, potentially causing the misclassification of water areas. For such cases, incorporating data from other SAR or optical remote sensing satellites can improve image correction. This study primarily employed S1 and S2 data, with limited use of the Landsat

and MODIS satellite series. Future studies could explore different regions and integrate higher-frequency observation satellites to improve data extraction accuracy.

Studies have indicated that the formation and outburst of the Kyagar Glacier lake are closely related to its unique geographical setting and local climate variations. Therefore, changes in water depth are not solely due to upstream outbursts. Outburst events typically occur in the summer, a period marked by high temperatures and mountain snowmelt. This season brings additional inflows from both sides of the valley, along with surrounding rockfalls, which can increase downstream water depth. We did not account for WSE changes due to non-upstream factors or depth reduction caused by deviations in the shallow water wave equations in the model. Furthermore, infiltration processes along downstream channels complicate accurate water depth predictions, adding aspects that are beyond the scope of hydrodynamic modeling. Long-term upstream erosion, coupled with floating ice and sediment transport, has resulted in relatively flat terrain with intricate flow pathways between the two glaciers. The formation of physical characteristics downstream still warrants further investigation.

The accuracy of water depth estimates derived using FwDET, lake volume calculations, and HEC-RAS dam breach simulations depends significantly on the choice of DEM. High-resolution DEMs enhance terrain detail, supporting more precise depth estimation. DEMs with greater vertical resolution can better capture local elevation changes, thus improving depth accuracy. DEMs are also crucial input data for HEC-RAS models, directly influencing key simulation outcomes, including water flow paths, channel morphology, flow distribution, and flood inundation extent. Counterintuitively, when using the ALOS DEM with a 12.5 m resolution in preliminary tests, the derived water depth estimations were inferior, achieving less than 82.1% coverage compared to the results presented in this study, which was more than 98.9% (Figure 7). This discrepancy underscores the importance of selecting an appropriate DEM dataset, which warrants further investigation.

In our model development process, we observed a distinctive characteristic related to flood events. Specifically, during weaker flood events associated with lower flow rates, the downstream water extent is generally shorter, and thus the impact on downstream communities is minimal. In contrast, during stronger flood events with higher flow rates (defined here as events with an average flow rate exceeding 132 m^3/s) our model indicates a 'stabilization' phenomenon in downstream water flow at around 130 m^3/s. At this threshold, the water extent reaches a point where it no longer expands significantly, suggesting that the model may be approaching an upper limit where the storage capacity within each grid cell reaches equilibrium. What causes this phenomenon, and how can the model be optimized to address it? These questions represent crucial areas for further exploration, particularly as this approach is applied to a broader range of case studies in the future.

5. Conclusions

Using remote sensing data from the Sentinel-1 and Sentinel-2 satellites, this study successfully delineated the water extent of the Kyagar Glacier lake before and after the outburst. By applying the FwDET, we derived water depth and volume changes, estimating an average outburst discharge of approximately 126.6 m^3/s. This estimated discharge provides a valuable reference for future hydrological analysis and model development related to glacial lake outburst floods (GLOFs). Additionally, understanding lake volume changes further enhances our knowledge of glacial lake dynamics. These results were integrated into a comprehensive GLOF model using HEC-RAS, combining FwDET-derived depth data with hydrodynamic simulations to assess downstream impacts of the outburst at different stages. From the initial breach until 05:36 am on 12 August 2018, the model estimated an average discharge between 120–140 m^3/s. Given that the latter range includes the estimated 126.6 m^3/s. The findings indicate that the Kyagar Glacier lake outburst was both rapid and destructive. The integration of remote sensing data and hydrodynamic modeling provided a thorough evaluation of the inundation extent, depth, and flow velocity downstream of the ice dam, offering insights valuable for future disaster management

and early warning systems. This study demonstrates an effective multi-tool approach to GLOF hazard assessment, underscoring the extensive potential of remote sensing and hydrodynamic modeling for disaster simulation.

Author Contributions: Conceptualization, L.J. and Z.L.; methodology, L.J.; software, L.J.; validation, L.J. and Z.L.; formal analysis, Z.L. and Z.Z.; investigation, L.J. and H.L.; resources, J.Z.; data curation, D.S.; writing-original draft preparation, L.J. and M.S.; writing—review and editing, L.J. and Z.L.; visualization, L.J and Z.Z. All authors have read and agreed to the published version of the manuscript.

Funding: This research was funded by the Second Tibetan Plateau Scientific Expedition and Research (STEP) Program (Grant No. 2019QZKK0103), the National Natural Science Foundation of China (Grant No. 42165006 and No. 42030611), and the Key R&D Plans of Tibet Autonomous Region in 2022 (Grandt No. XZ202201ZY0008G).

Data Availability Statement: The Sentinel satalite data are available from https://dataspace.copernicus.eu/ (accessed on 27 October 2024). The ASTGTM v003 are available from https://search.earthdata.nasa.gov/ (accessed on 27 October 2024).

Acknowledgments: The authors thank the European Space Agency (ESA) satellite missions for providing satellite data support for this study, as well as NASA and the Japan Aerospace Exploration Agency (JAXA) for jointly developing and making publicly available digital elevation models. The glcaier data set is provided by National Tibetan Plateau/Third Pole Environment Data Center (http://data.tpdc.ac.cn (accessed on 26 October 2024)). We would also thank many anonymous contributors for their technical and financial support. The authors thank Planet Labs for Planet and RapidEye datasets, Japan Aerospace Exploration Agency (JAXA) and European Space Agency (ESA) for ALOS-1 PALSAR-1 and ALOS-2 PALSAR-2 data, and Qinghai-Tibet Plateau ground monitoring station for metrological data. We also thank the editor and anonymous reviewers for their helpful comments and suggestions.

Conflicts of Interest: The authors declare no conflicts of interest.

References

1. Ding, Y.K.; Feng, Y.Q.; Chen, K.; Zhang, X.C. Analysis of spatial and temporal changes in vegetation cover and its drivers in the aksu river basin, china. *Sci. Rep.* **2024**, *14*, 15. [CrossRef] [PubMed]
2. Intergovernmental Panel on Climate Change (IPCC). *Climate Change 2022—Impacts, Adaptation and Vulnerability: Working Group II Contribution to the Sixth Assessment Report of the Intergovernmental Panel on Climate Change*; Cambridge University Press: Cambridge, UK, 2023.
3. Hugonnet, R.; McNabb, R.; Berthier, E.; Menounos, B.; Nuth, C.; Girod, L.; Farinotti, D.; Huss, M.; Dussaillant, I.; Brun, F.; et al. Accelerated global glacier mass loss in the early twenty-first century. *Nature* **2021**, *592*, 726. [CrossRef] [PubMed]
4. Zemp, M.; Huss, M.; Thibert, E.; Eckert, N.; McNabb, R.; Huber, J.; Barandun, M.; Machguth, H.; Nussbaumer, S.U.; Gärtner-Roer, I.; et al. Global glacier mass changes and their contributions to sea-level rise from 1961 to 2016. *Nature* **2019**, *568*, 382–386. [CrossRef] [PubMed]
5. Yin, Y.; Wang, X.; Liu, S. Characteristics and influence factors of the glacial lake changes in china from 1990 to 2020. *J. Lake Sci.* **2023**, *35*, 358–367.
6. Tang, M.; Chen, H.; Zhao, H.; Yang, W.; Deng, W. Identification, development law and risk assessment of the hidden dangers of glacial lake outburst disasters on the qinghai-tibet plateau. *Geol. Bull. China* **2023**, *42*, 730–742.
7. Liu, X.; Chen, B. Climatic warming in the tibetan plateau during recent decades. *Int. J. Climatol. J. R. Meteorol. Soc.* **2000**, *20*, 1729–1742. [CrossRef]
8. Rangwala, I.; Miller, J.R.; Xu, M. Warming in the tibetan plateau: Possible influences of the changes in surface water vapor. *Geophys. Res. Lett.* **2009**, *36*, L06703. [CrossRef]
9. Tang, S.; Vlug, A.; Piao, S.; Li, F.; Wang, T.; Krinner, G.; Li, L.Z.; Wang, X.; Wu, G.; Li, Y. Regional and tele-connected impacts of the tibetan plateau surface darkening. *Nat. Commun.* **2023**, *14*, 32. [CrossRef]
10. Zhang, G.; Carrivick, J.L.; Emmer, A.; Shugar, D.H.; Veh, G.; Wang, X.; Labedz, C.; Mergili, M.; Mölg, N.; Huss, M.; et al. Characteristics and changes of glacial lakes and outburst floods. *Nat. Rev. Earth Environ.* **2024**, *5*, 447–462. [CrossRef]
11. Peng, M.; Wang, X.; Zhang, G.; Veh, G.; Sattar, A.; Chen, W.; Allen, S. Cascading hazards from two recent glacial lake outburst floods in the nyainqêntanglha range, tibetan plateau. *J. Hydrol.* **2023**, *626*, 130155. [CrossRef]
12. Chen, L.; Fan, X.; Xiong, J.; Wang, X.; Dou, X. Hazard assessment of glacial lake outbursts in the doyinongba basin, southeastern tibetan plateau. *Bull. Geol. Sci. Technol.* **2023**, *42*, 258–266.

13. Ren, S.; Jiang, L.; Zhai, S.; Ye, X.; Guo, J. Study on erosion evolution characteristics of glacial lake break flood based on dynamic process. *J. Glaciol. Geocryol.* **2023**, *45*, 1300–1313.
14. Yu, Y.; Li, B.; Li, Y.; Jiang, W. Retrospective analysis of glacial lake outburst flood (glof) using ai earth insar and optical images: A case study of south lhonak lake, sikkim. *Remote Sens.* **2024**, *16*, 2307. [CrossRef]
15. Taylor, C.; Robinson, T.R.; Dunning, S.; Rachel Carr, J.; Westoby, M. Glacial lake outburst floods threaten millions globally. *Nat. Commun.* **2023**, *14*, 487. [CrossRef] [PubMed]
16. Emmer, A.; Allen, S.K.; Carey, M.; Frey, H.; Huggel, C.; Korup, O.; Mergili, M.; Sattar, A.; Veh, G.; Chen, T.Y.; et al. Progress and challenges in glacial lake outburst flood research (2017–2021): A research community perspective. *Nat. Hazards Earth Syst. Sci. Discuss.* **2022**, *22*, 3041–3061. [CrossRef]
17. Luo, H.; Lin, Z.; Chen, H.; Xiao, D.; Chen, G.; Su, D. Assessments of multiple precipitation products and application in hydrodynamic simulations: A case of casualty-inducing mountain torrents in Sichuan, southwest China. *J. Flood Risk Manag.* **2024**, *17*, e13016. [CrossRef]
18. Su, L.-f.; Li, Z.; Gao, F.; Yu, M. A review of remote sensing image water extraction. *Remote Sens. Land Resour.* **2021**, *33*, 9–19.
19. Gu, C.; Li, S.; Liu, M.; Hu, K.; Wang, P. Monitoring glacier lake outburst flood (glof) of lake Merzbacher using dense Chinese high-resolution satellite images. *Remote Sens.* **2023**, *15*, 1941. [CrossRef]
20. Gao, Y.; Yang, W.; Guo, R.; Jiang, L. Remote sensing monitoring and analysis of Jinwuco lateral moraine landslide-glacial lake outburst in southeast Tibet. *Remote Sens.* **2023**, *15*, 1475. [CrossRef]
21. Yang, L.; Lu, Z.; Ouyang, C.; Zhao, C.; Hu, X.; Zhang, Q. Glacial lake outburst flood monitoring and modeling through integrating multiple remote sensing methods and hec-ras. *Remote Sens.* **2023**, *15*, 5327. [CrossRef]
22. Sattar, A.; Goswami, A.; Kulkarni, A.V. Application of 1d and 2d hydrodynamic modeling to study glacial lake outburst flood (glof) and its impact on a hydropower station in central Himalaya. *Nat. Hazards* **2019**, *97*, 535–553. [CrossRef]
23. Tunyaz, N.; Mijit, M.; Weiyi, M.; Mijit, M.; Zhang, A.; Liu, Y. Variation characteristics of kyagar glacial lake outburst floods in the yarkand river basin from 1961 to 2021. *J. Glaciol. Geocryol.* **2023**, *45*, 1288–1299.
24. Jingrong, W. Investigation and analysis on the causes of sudden glacial floods in the yarkand river of xinjiang. *Bull. Soiland Water Conserv.* **1990**, *10*, 33–38.
25. Haemmig, C.; Huss, M.; Keusen, H.; Hess, J.; Wegmüller, U.; Ao, Z.; Kulubayi, W. Hazard assessment of glacial lake outburst floods from Kyagar glacier, Karakoram mountains, China. *Ann. Glaciol.* **2014**, *55*, 34–44. [CrossRef]
26. Gao, Y.; Wang, J.; Liu, S.; Yao, X.; Qi, M.; Liang, P.; Xie, F.; Mu, J.; Ma, X. Monitoring dynamics of kyagar glacier surge and repeated draining of ice-dammed lake using multi-source remote sensing. *Sci. Total Environ.* **2024**, *928*, 172467. [CrossRef] [PubMed]
27. Feng, Q. Characteristics of glacier outburst flood in the yarkant river, karakorum mountains. *GeoJournal* **1991**, *25*, 255–263. [CrossRef]
28. Round, V.; Leinss, S.; Huss, M.; Haemmig, C.; Hajnsek, I. Surge dynamics and lake outbursts of Kyagar glacier, Karakoram. *Cryosphere* **2017**, *11*, 723–739. [CrossRef]
29. Li, G.; Lv, M.; Quincey, D.J.; Taylor, L.S.; Li, X.; Yan, S.; Sun, Y.; Guo, H. Characterizing the surge behaviour and associated ice-dammed lake evolution of the Kyagar glacier in the Karakoram. *Cryosphere* **2023**, *17*, 2891–2907. [CrossRef]
30. Liu, J.; Milne, R.I.; Zhu, G.-F.; Spicer, R.A.; Wambulwa, M.C.; Wu, Z.-Y.; Boufford, D.E.; Luo, Y.-H.; Provan, J.; Yi, T.-S.; et al. Name and scale matter: Clarifying the geography of tibetan plateau and adjacent mountain regions. *Glob. Planet. Chang.* **2022**, *215*, 103893. [CrossRef]
31. Guo, W.; Liu, S.; Xu, J.; Wu, L.; Shangguan, D.; Yao, X.; Wei, J.; Bao, W.; Yu, P.; Liu, Q.; et al. The second Chinese glacier inventory: Data, methods and results. *J. Glaciol.* **2015**, *61*, 357–372. [CrossRef]
32. Liu, S.; Yao, X.; Guo, W.; Xu, J.; Shangguan, D.; Wei, J.; Bao, W.; Wu, L. The contemporary glaciers in china based on the second chinese glacier inventory. *Acta Geogr. Sin.* **2015**, *70*, 3–16.
33. Torres, R.; Snoeij, P.; Geudtner, D.; Bibby, D.; Davidson, M.; Attema, E.; Potin, P.; Rommen, B.; Floury, N.; Brown, M. Gmes sentinel-1 mission. *Remote Sens. Environ.* **2012**, *120*, 9–24. [CrossRef]
34. Drusch, M.; Del Bello, U.; Carlier, S.; Colin, O.; Fernandez, V.; Gascon, F.; Hoersch, B.; Isola, C.; Laberinti, P.; Martimort, P. Sentinel-2: Esa's optical high-resolution mission for gmes operational services. *Remote Sens. Environ.* **2012**, *120*, 25–36. [CrossRef]
35. Feng, Q.; Wang, Q.; Huang, H.; Wang, Z. Improved otsu algorithm for water extraction based on sentinel-1 dual-polarization data. *Remote Sens. Technol. Appl.* **2022**, *37*, 1003–1011.
36. Gao, B.-C. Normalized difference water index for remote sensing of vegetation liquid water from space. In *Imaging Spectrometry*; SPIE: Bellingham, WA, USA, 1995; pp. 225–236.
37. Du, Y.; Zhang, Y.; Ling, F.; Wang, Q.; Li, W.; Li, X. Water bodies' mapping from sentinel-2 imagery with modified normalized difference water index at 10-m spatial resolution produced by sharpening the swir band. *Remote Sens.* **2016**, *8*, 354. [CrossRef]
38. Cohen, S.; Raney, A.; Munasinghe, D.; Loftis, J.D.; Molthan, A.; Bell, J.; Rogers, L.; Galantowicz, J.; Brakenridge, G.R.; Kettner, A.J.; et al. The floodwater depth estimation tool (fwdet v2. 0) for improved remote sensing analysis of coastal flooding. *Nat. Hazards Earth Syst. Sci.* **2019**, *19*, 2053–2065. [CrossRef]
39. Cohen, S.; Brakenridge, G.R.; Kettner, A.; Bates, B.; Nelson, J.; McDonald, R.; Huang, Y.F.; Munasinghe, D.; Zhang, J. Estimating floodwater depths from flood inundation maps and topography. *JAWRA J. Am. Water Resour. Assoc.* **2018**, *54*, 847–858. [CrossRef]

40. Peter, B.G.; Cohen, S.; Lucey, R.; Munasinghe, D.; Raney, A.; Brakenridge, G.R. Google earth engine implementation of the floodwater depth estimation tool (fwdet-gee) for rapid and large scale flood analysis. *IEEE Geosci. Remote Sens. Lett.* **2020**, *19*, 1501005. [CrossRef]
41. Parida, B.R.; Tripathi, G.; Pandey, A.C.; Kumar, A. Estimating floodwater depth using sar-derived flood inundation maps and geomorphic model in kosi river basin (india). *Geocarto Int.* **2022**, *37*, 4336–4360. [CrossRef]
42. Cohen, S.; Peter, B.G.; Haag, A.; Munasinghe, D.; Moragoda, N.; Narayanan, A.; May, S. Sensitivity of remote sensing floodwater depth calculation to boundary filtering and digital elevation model selections. *Remote Sens.* **2022**, *14*, 5313. [CrossRef]
43. Sattar, A.; Haritashya, U.K.; Kargel, J.S.; Leonard, G.J.; Shugar, D.H.; Chase, D.V. Modeling lake outburst and downstream hazard assessment of the lower barun glacial lake, nepal himalaya. *J. Hydrol.* **2021**, *598*, 126208. [CrossRef]
44. Leoul, A.; Kassahun, N. Dam breach analysis using hec-ras and hec-georas: The case of kesem kebena dam. *Open J. Mod. Hydrol.* **2019**, *9*, 113–142. [CrossRef]
45. Thun, L.J.V.; Gillette, D.R. *Guidance on Breach Parameters*; U.S. Department of the Interior, Bureau of Reclamation: Washington, DC, USA, 1990.
46. Limerinos, J.T. *Determination of the Manning Coefficient from Measured Bed Roughness in Natural Channels*; US Government Printing Office: Washington, DC, USA, 1970.
47. Tang, W.; Zhou, Q.; Liu, X.; Zhu, W.; Mao, X. Anlyisis on verification of national severe convective weather categorical forecasts. *J. Meteorol. Res.* **2017**, *43*, 67–76.
48. Casati, B.; Wilson, L.; Stephenson, D.; Nurmi, P.; Ghelli, A.; Pocernich, M.; Damrath, U.; Ebert, E.; Brown, B.; Mason, S. Forecast verification: Current status and future directions. *Meteorol. Appl. J. Forecast. Pract. Appl. Train. Tech. Model.* **2008**, *15*, 3–18. [CrossRef]
49. Lin, Z.; Yao, X.; Du, J.; Zhou, Z. Refined evaluation of satellite precipitation products against rain gauge observations along the sichuan—Tibet railway. *J. Meteorol. Res.* **2022**, *36*, 779–797. [CrossRef]
50. Cao, C.; Chen, K.; Chen, Y.; Liu, J.; Chen, J.; He, J.; Chen, X. A novel method of error evaluation for radar nowcasting based on shape matching. *J. Meteorol. Res.* **2017**, *43*, 987–997.
51. Peng, L.; Ao, Z.; Yuan, B.; Jiang, H. Study on volume interpolation calculation of kyagar glacier lake based on dem. *Yellow River* **2015**, *37*, 21–23.
52. Zhang, Z.; Zhao, J.; Liu, S.; Zhang, Q.; Jiang, Z.; Xu, Y.; Su, H. Characterization of three surges of the kyagar glacier, karakoram. *Remote Sens.* **2023**, *15*, 2113. [CrossRef]
53. Wang, G.; Hu, Y.; Zhang, S.; Ru, Y.; Chen, K.; Wu, M. Water identification from the gf-1 satellite image based on the deep convolutional neural networks. *Natl. Remote Sens. Bull.* **2022**, *26*, 2304–2316. [CrossRef]

Disclaimer/Publisher's Note: The statements, opinions and data contained in all publications are solely those of the individual author(s) and contributor(s) and not of MDPI and/or the editor(s). MDPI and/or the editor(s) disclaim responsibility for any injury to people or property resulting from any ideas, methods, instructions or products referred to in the content.